JVST A
Journal of Vacuum Science & Technology A
ARTICLE
pubs.aip.org/avs/jva

Ultrathin ZrO_2 thickness control on TiO_2/ZrO_2 core/shell nanoparticles using ZrO_2 atomic layer deposition and etching

Cite as: J. Vac. Sci. Technol. A **42**, 052604 (2024); doi: 10.1116/6.0003781
Submitted: 24 May 2024 · Accepted: 15 July 2024 ·
Published Online: 20 August 2024

View Online Export Citation CrossMark

Janine D. Sempel,[1] Marja-Leena Kaariainen,[1] Troy A. Colleran,[1] Alejo M. Lifschitz,[2] and Steven M. George[1,a)]

AFFILIATIONS

[1] Department of Chemistry, University of Colorado, Boulder, Colorado 80309
[2] Meta Reality Labs, 9845 Willows Rd NE, Redmond, Washington 98052

Note: This paper is part of the 2025 Special Topic Collection on Atomic Layer Etching (ALE).

[a)] **Author to whom correspondence should be addressed:** Steven.George@colorado.edu

ABSTRACT

Atomic layer deposition (ALD) and atomic layer etching (ALE) techniques were used to control the ZrO_2 shell thickness on TiO_2/ZrO_2 core/shell nanoparticles. ALD and ALE were performed at 200 °C while the nanoparticles were agitated using a rotary reactor. To increase the ZrO_2 shell thickness, ZrO_2 ALD films were deposited using sequential exposures of tetrakis(dimethylamino) zirconium and H_2O. *Ex situ* analysis using transmission electron microscopy (TEM) observed the growth of the ZrO_2 shells. The ZrO_2 ALD led to more spherical ZrO_2 shells on the crystalline and irregular TiO_2 cores. The ZrO_2 ALD on the nanoparticles had a growth rate of 0.9 ± 0.1 Å/cycle. Tunable ZrO_2 coatings were observed with thicknesses ranging from 5.9 to 27.1 nm after 240 ZrO_2 ALD cycles. To demonstrate the decrease in the ZrO_2 shell thickness, the ZrO_2 film was then etched using sequential hydrogen fluoride (HF) and $TiCl_4$ exposures. Quadrupole mass spectrometry experiments performed in a separate reactor identified the volatile products during ZrO_2 ALE. H_2O was monitored during HF exposures, and $ZrCl_4$ etch products and TiF_xCl_y ligand-exchange products were observed during $TiCl_4$ exposures. *Ex situ* TEM studies revealed that the ZrO_2 shells remained spherical during ZrO_2 ALE. The ZrO_2 ALE on the nanoparticles had an etch rate of 6.5 ± 0.2 Å/cycle. Tunable ZrO_2 coatings were produced from 27.1 down to 7.6 nm using 30 ZrO_2 ALE cycles. This study demonstrated that ZrO_2 ALD and ZrO_2 ALE can control the thickness of ZrO_2 shells on TiO_2/ZrO_2 core/shell nanoparticles without inducing nanoparticle agglomeration.

I. INTRODUCTION

Controlling the layered structure of multicomponent core/shell nanoparticles is an active area of research. Core/shell nanoparticles have a central core material that is encapsulated by a shell of a different material.[1] The shell allows nanoparticles to be engineered with the surface properties of the shell and the bulk properties of the core.[1,2] Varying the shell material on the core material also provides an avenue to alter the properties of the core material.[1,3,4] Changing the thickness of the thin shell on the underlying core leads to tunable nanoparticle properties.[5,6] Synthetic techniques are needed to control the shell thickness without causing nanoparticle agglomeration.[7]

Ultrathin shells on nanoparticles can be deposited using atomic layer deposition (ALD) techniques.[8,9] ALD is a gas-phase process related to chemical vapor deposition (CVD) that splits a binary CVD reaction into two sequential, self-limiting surface reactions.[8] ALD has been used to coat nanoparticles.[9] The first successful demonstration of conformal ALD films on nanoparticles was Al_2O_3 ALD on BN nanoparticles.[10] Many other examples of ALD films on nanoparticles or micrometer-sized particles have subsequently been demonstrated using a variety of ALD chemistries and types of particles.[11–15]

ALD can have initial nucleation difficulties that lead to gaps in the initial coating.[16] One strategy to obtain ultrathin and more continuous films is to combine ALD and thermal atomic layer etching (ALE).[16] Thermal ALE can be viewed as the reverse of ALD.[17,18] ALE is based on self-limiting, binary surface reaction sequences that remove the material from the surface.[17] One reaction typically modifies the initial surface. The second reaction then volatilizes the modified surface layer. Thermal ALE methods have been introduced for a number of materials including various oxides, nitrides, metals, and semiconductors.[17,19]

ALD and thermal ALE can be used together to obtain thinner and more continuous films than films fabricated with ALD alone. Thicker ALD films can eventually fill the initial gaps in the coating. ALE can then etch this thicker ALD film back to obtain a more continuous ultrathin film.[16] A schematic of this deposition and etchback approach on particles is illustrated in Fig. 1. An earlier application of the deposition and etchback approach employed Al_2O_3 ALD and Al_2O_3 ALE to obtain ultrathin and more continuous films for metal-insulator-metal (MIM) capacitors.[16]

TiO_2 nanoparticles have important applications for photocatalysis, photovoltaics, pigments, and sunscreen, and as a filler for high refractive index optical coatings.[20–22] Ultrathin and continuous shells on core TiO_2 nanoparticles are important to functionalize the surface of these nanoparticles. For example, the shell can improve the dispersion of the core/shell nanoparticles in TiO_2/polymer composites.[23] TiO_2/polymer composites can have much higher refractive indices than the original polymer.[24–26] The refractive index of typical polymers is $n \sim 1.5$. The refractive index of TiO_2/polymer composites can vary from $n = 1.5$ to $n = 1.9$.[24–26]

One problem with introducing TiO_2 nanoparticles into polymers to form TiO_2/polymer composites is the photocatalytic degradation of the polymer.[27–29] Excitation of the TiO_2 can create electron/hole pairs in TiO_2 that can promote reactions that lead to polymer degradation.[29] This degradation can be polymer decomposition or polymer discoloration that compromises the quality and transparency of the TiO_2/polymer composite.[27,29] This polymer degradation can be prevented by depositing continuous protective shells on the TiO_2 nanoparticles.[28,29]

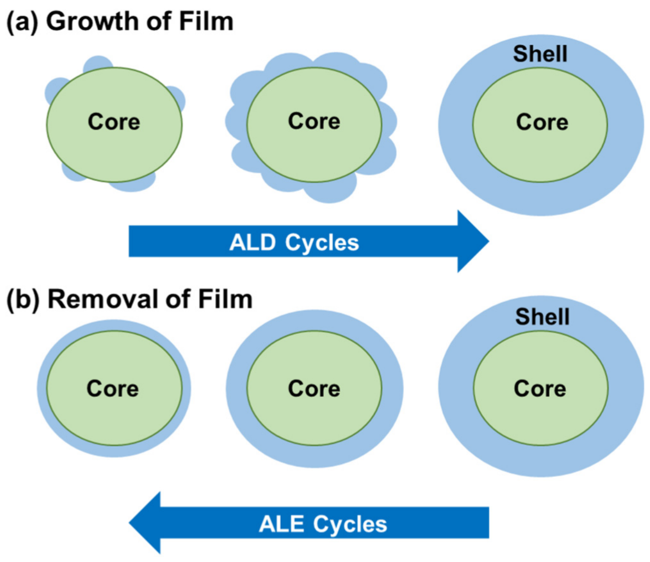

FIG. 1. (a) ALD growth on the core nanoparticle yields a thicker, continuous shell after multiple ALD cycles. (b) ALE of the shell on the core nanoparticle reduces the shell thickness and produces a thinner, continuous shell after multiple ALE cycles.

In this paper, ZrO_2 ALD films were deposited on TiO_2/ZrO_2 core/shell nanoparticles using alternating exposures of tetrakis (dimethylamino)zirconium (TDMAZ) and water.[30,31] This ZrO_2 ALD chemistry using TDMAZ and H_2O has also been previously employed to coat particles and other porous materials.[32–35] The ZrO_2 ALD films on the ZrO_2/TiO_2 core/shell nanoparticles were then etched back using ZrO_2 ALE with alternating exposures of hydrogen fluoride (HF) and $TiCl_4$.[36,37] For both ZrO_2 ALD and ZrO_2 ALE, transmission electron microscopy (TEM) was used to monitor the growth and etching of the ZrO_2 thin shells. The TEM results provide a proof-of-concept that ZrO_2 ALD and ZrO_2 ALE can control the thickness of the ZrO_2 shells on TiO_2/ZrO_2 core/shell nanoparticles without inducing nanoparticle agglomeration.

II. EXPERIMENT

A. Rotary reactor for particle ALD and ALE

A rotary reactor was utilized for the particle ALD and ALE. A schematic of the rotary reactor is given in Fig. 2.[38,39] The TiO_2/ZrO_2 core/shell nanoparticles were purchased from Nanoshel (nanoshel.com). The as-received TiO_2/ZrO_2 core/shell nanoparticles were housed in the rotary reactor in a stainless-steel closed-end rotating cylinder with porous walls that was mounted onto a magnetic feed-through.[38–40] The mass of nanoparticles added to the rotary reactor was ∼1.0 g. The magnetic feed-through rotated the stainless-steel cylinder at 50 rpm. The cylindrical canister was 3 in. in diameter and 8 in. in length. The nanoparticles were constantly agitated and moving in a cascading motion during ALD and ALE.[38]

Reactants were dosed through valves that prevented the reactants from mixing until they were introduced into the reactor. A gate valve separated the pump from the rotary reactor. Closing this gate valve allowed for static reactant exposures. Static exposures were used to increase the contact time between the precursors and the nanopowder. A Baratron capacitance manometer was attached to the

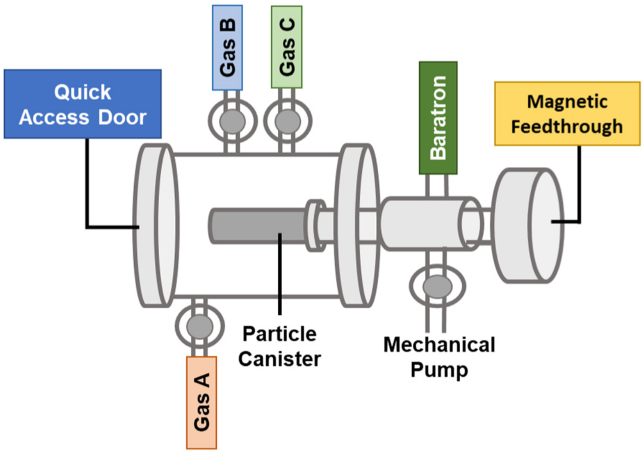

FIG. 2. Schematic of the rotary reactor for particle ALD and ALE. Nanoparticles are housed in a canister that rotates to agitate the nanopowder during ALD and ALE.

reactor to monitor the pressure changes that occurred inside the reactor. A mechanical pump was used to maintain a base pressure of <30 mTorr in the reactor.

B. Reaction conditions for ZrO_2 ALD and ZrO_2 ALE

The ZrO_2 films were deposited and etched in the rotary reactor. The ALD reactions were performed at 200 °C using static, sequential exposures of TDMAZ (99.99%, Sigma-Aldrich) and de-ionized (DI) H_2O as reactants.[30,31] Prior to ZrO_2 ALD processing, the as-received nanoparticles were held in vacuum at 200 °C for 30 min. TDMAZ was heated and held at 80 °C. H_2O was kept at ambient temperature. Nitrogen (UHP, Airgas, Radnor, PA) was used to purge the system between reactant doses. Figure 3(a) illustrates the ZrO_2 ALD process and reaction products.

An estimate of the surface area of the TiO_2/ZrO_2 core/shell nanoparticles can be determined from the mass and diameter of the nanoparticles. The total nanoparticle mass is ~1.0 g. Assuming that the nanoparticles are composed primarily of TiO_2, the TiO_2 volume is 0.235 cm^3. The average nanoparticle diameter is 53.5 nm. Based on this diameter and assuming that the nanoparticles are spherical, the TiO_2 volume is composed of $\sim 3 \times 10^{15}$ nanoparticles loaded in the rotary reactor. These spherical nanoparticles would have a total surface area of ~26 m^2.

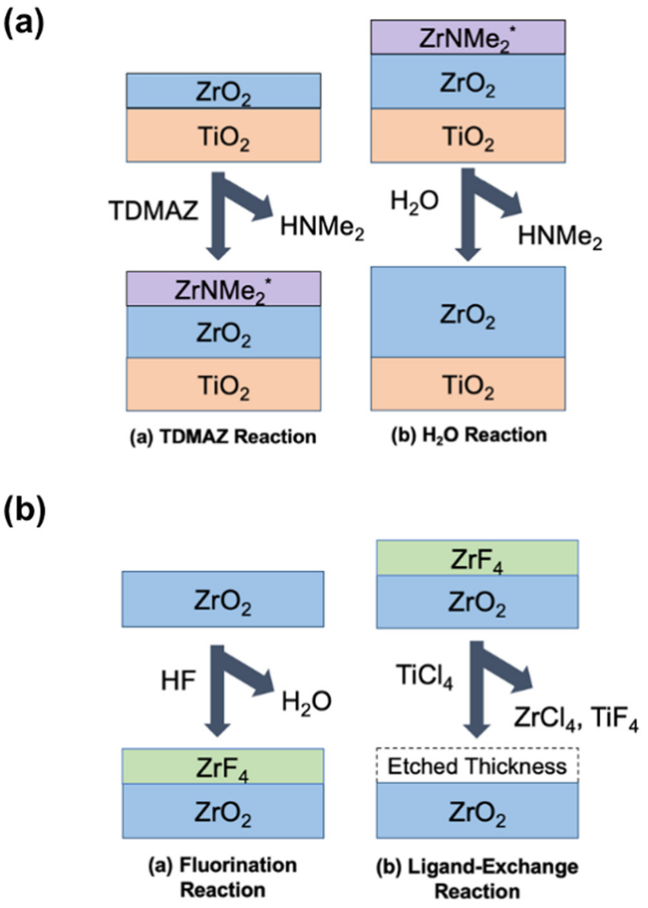

FIG. 3. (a) Mechanism for ZrO_2 ALD based on sequential reactions of TDMAZ and H_2O. (b) Mechanism for ZrO_2 ALE based on sequential reactions of HF for fluorination and $TiCl_4$ for ligand-exchange.

Due to the high surface area of the powders, static precursor exposures were used to facilitate complete reactions with all the surface sites for the ZrO_2 ALD and ZrO_2 ALE at 200 °C. Multiple micropulse dosing was used to define the reactant exposures. A typical dosing scheme for the growth of ZrO_2 ALD films was as follows: three TDMAZ micropulses at ~0.25 Torr for 15 s, N_2 purge for 130 s, three H_2O micropulses at ~0.5 Torr for 20 s, and N_2 purge for 130 s.

In the first reaction, TDMAZ was dosed and reacts with the hydroxyl groups on the film surface. This reaction deposits $Zr(NMe_2)_3^*$ groups on the surface. In the second step, H_2O reacts with the $Zr(NMe_2)_3^*$ species and returns hydroxyl groups on surface. The hydroxyl groups are not explicitly shown in Fig. 3(a). In both reactions, $HNMe_2$ is the volatile product. The reactions were repeated sequentially to deposit the ZrO_2 ALD coating. This ZrO_2 ALD chemistry is known to deposit ZrO_2 at a rate of 0.8 Å/cycle at 225 °C.[31]

After the completion of the ZrO_2 ALD cycles, the ZrO_2 ALE reactions were performed at 200 °C using static, sequential micropulses of hydrogen fluoride and titanium tetrachloride (99.9%, ThermoFisher Scientific).[36,37] Nitrogen (UHP, Airgas, Radnor, PA) was used to purge the system between reactant doses. The proposed mechanism for ZrO_2 ALE using HF for fluorination and $TiCl_4$ for ligand exchange is shown in Fig. 3(b).

In the first reaction, HF fluorinates the ZrO_2 nanoparticles and produces a ZrF_4 layer on the surface and H_2O as a volatile product. In the second reaction, $TiCl_4$ undergoes ligand exchange with the ZrF_4 layer to produce $ZrCl_4$ as the volatile etch product. A typical dosing scheme for etching the ZrO_2 films was as follows: four HF micropulses at ~0.8 Torr for 0.3 s, N_2 purge for 230 s, four $TiCl_4$ micropulses at ~1 Torr for 0.3 s, and N_2 purge for 230 s.

C. Mass spectrometry studies of ZrO_2 ALE

Quadrupole mass spectrometry (QMS) studies of ZrO_2 ALE were performed in a separate reactor that uses high surface area powder to obtain sufficient sensitivity.[41,42] Alternating exposures of the ALE precursors were flowed over the powder in the sample holder. The precursors enter through separate inlet lines that end just before the powder sample holder.[42] After the precursors react with the powder surface, the etch products are transported out of the sample holder by N_2 carrier gas. Some of the gas stream passes through an aperture and undergoes a molecular beam expansion into vacuum. The molecular beam is then intercepted by a skimmer that allows the center of the molecular beam to reach the QMS ionizer.[41,42]

ZrO_2 powders (High Purity, 99.9%, US-Nano) with diameters of ~100 nm and typical powder masses between 30 and 40 mg were loaded into the sample holder. The ultrahigh purity N_2 carrier gas through the two reactant manifolds produced a pressure of ~2.7 Torr in the sample holder. The N_2 gas acts as both a carrier gas for the etch products and a purge gas. The HF and $TiCl_4$ reactants were flowed through the sample holder at ~4.0 Torr. Experiments were conducted using 120 s exposures of the precursor gases. These exposures were followed by 300 s purge times to remove the previous precursor from the powder bed. The temperature of the powder bed was controlled at 200, 250, or 300 °C.

The etch products were analyzed using a quadrupole mass spectrometer (Extrel MAX-QMS flange-mounted system).[41,42] The experimentally measured mass spectra were compared with the theoretical relative abundance expected for each *m/z* value. The isotopic distributions were determined from the naturally occurring isotopic abundances of each element present in the etch products. Some *m/z* values might contain contributions from more than one distinct etch product.

D. Powder x-ray diffraction, TEM measurements, and XPS analysis

Powder x-ray diffraction (PXRD) analysis of the TiO_2/ZrO_2 core/shell nanoparticles was performed using a Bruker AXS D8 Advance A25 instrument. TEM measurements were conducted using a FEI Tecnai T12 Spirit 120 kV instrument. The TEM was operated at 100 kV in the bright-field mode. Samples were prepared by suspending the particles in isopropanol and pipetting a few drops of the suspension onto Cu TEM grids that were supported with carbon.

X-ray photoelectron spectroscopy was performed on the as-received TiO_2/ZrO_2 core/shell nanoparticles samples using a PHI 5600 instrument. A monochromatic Al Kα source (1486.6 eV) was used to collect survey scans with a pass energy of 93.9 eV and a step size of 0.4 eV/step. All spectra were referenced to the adventitious carbon peak centered at 285 eV. The XPS data were collected using Auger Scan (RBD Instruments) software and analyzed using CasaXPS.

III. RESULTS AND DISCUSSION

A. Substrate and substrate characterization

The TiO_2/ZrO_2 core/shell nanoparticles from Nanoshel were analyzed using TEM. Starting with the as-received TiO_2/ZrO_2 core/shell nanoparticles was necessary because initial TiO_2 nanoparticles are severely agglomerated. The nanoparticles were measured using ImageJ software to determine the size distribution of the TiO_2 cores and the ZrO_2 shells on the nanoparticles. The size distribution of the TiO_2 core ranged from 20 to 70 nm and the ZrO_2 shell ranged from 3 to 11 nm. PXRD measurements of the TiO_2/ZrO_2 core/shell nanoparticles showed that the TiO_2 core nanoparticles were crystalline. The PXRD results indicated that the TiO_2 crystal structure was hexagonal based on diffraction peaks at 35, 38, 41, 53, 58, and 63°. The ZrO_2 shell did not display any crystallinity.

A TEM image of the as-received TiO_2/ZrO_2 core/shell nanoparticles is shown in Fig. 4(a). The TiO_2 core is apparent as the light gray interior, and the ZrO_2 shell is visible as the darker gray coating. Figure 4(b) shows the histogram distribution of the ZrO_2 shell thickness on the as-received TiO_2/ZrO_2 core/shell nanoparticles. Measurements were recorded for one hundred individual nanoparticles from the as-received nanoparticles. One ZrO_2 shell thickness measurement was recorded if the ZrO_2 shell was uniform on the TiO_2 core. If the ZrO_2 shell thickness was not uniform, the extremes of the ZrO_2 shell thickness were recorded and then averaged to obtain the ZrO_2 shell thickness. The as-received nanoparticles had an average TiO_2 core diameter of 41.7 ± 11.4 nm and an average ZrO_2 shell thickness of 5.9 ± 1.8 nm.

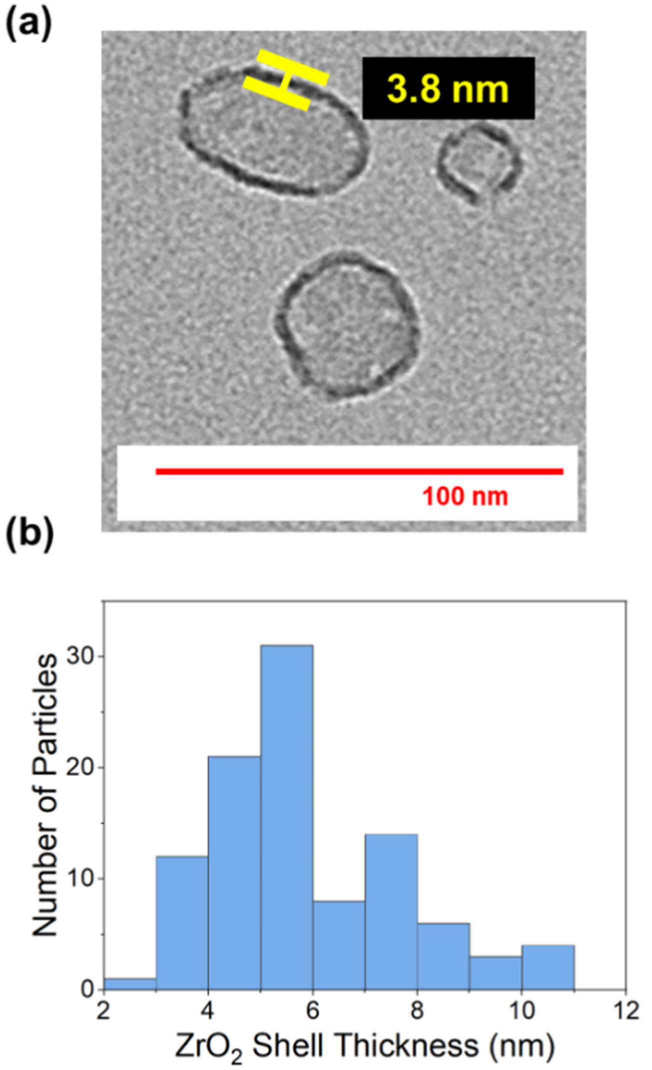

FIG. 4. (a) TEM images of as-received TiO_2/ZrO_2 core/shell nanoparticles from Nanoshel. (b) Histogram of ZrO_2 shell thickness distribution from TEM measurements on 100 as-received TiO_2/ZrO_2 core/shell nanoparticles.

Additionally, Fig. 5 shows that the as-received TiO_2/ZrO_2 core/shell nanoparticles from Nanoshel were observed individually and were not aggregated in agglomerates. In contrast, TiO_2 nanoparticles with no coating were found to form large agglomerates and were difficult to disperse.[43,44] TiO_2 agglomerates have also been found to change the performance of TiO_2 nanoparticles.[45,46]

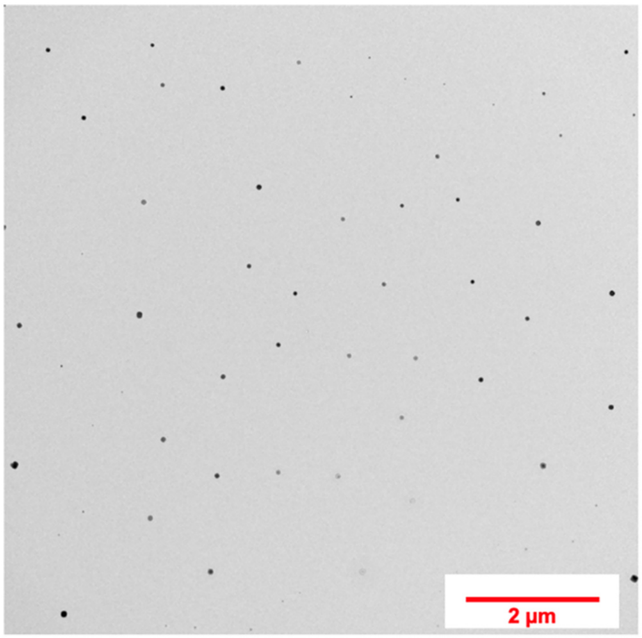

FIG. 5. Distribution of as-received TiO_2/ZrO_2 core/shell nanoparticles from Nanoshel imaged by TEM showing individual nanoparticles without agglomeration.

The monodispersed TiO_2/ZrO_2 core/shell nanoparticles from Nanoshel were important for this proof-of-concept study to demonstrate that ZrO_2 ALD and ZrO_2 ALE could control the shell thicknesses on TiO_2/ZrO_2 core/shell nanoparticles.

XPS analysis was also performed on the as-received TiO_2/ZrO_2 core/shell nanoparticles from Nanoshel. The XPS survey spectra conducted without any initial surface sputtering revealed the expected XPS peaks for Zr 3d (9.66 at. %), Zr 3p (8.07 at. %), Ti 2p (1.53 at. %), and O 1s (36.15 at. %). In addition, XPS peaks for C 1s (39.15 at. %), Na 1s (0.72 at. %), Fe 2p (1.94 at. %), and Cl 2p (2.84 at. %) were observed from surface contaminants.

B. Pressure measurements during ZrO_2 ALD

Multiple micropulses were used to define the exposures for the ZrO_2 ALD. The pressure measurements during these micropulses characterize the self-limiting nature of the ALD reactions.[8] The pressure recorded for multiple micropulses during the TDMAZ reaction with the TiO_2/ZrO_2 core/shell nanoparticles at 200 °C is shown in Fig. 6(a). These results were obtained during the 45th ALD cycle. Repetitive micropulses of TDMAZ at pressures of ~0.15 Torr were used for these experiments.

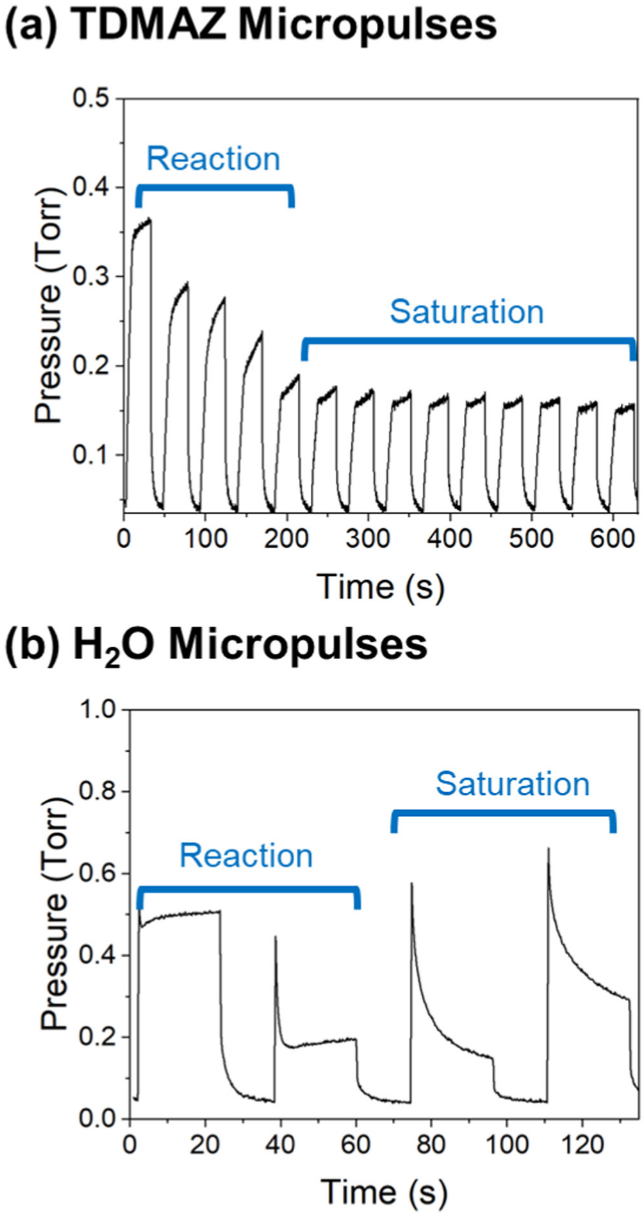

FIG. 6. Transient pressure measurements for multiple micropulses during ZrO_2 ALD at 200 °C during the 45th ALD cycle showing reaction and saturation regimes for (a) TDMAZ and (b) H_2O.

The first four micropulses labeled "Reaction" in Fig. 6(a) show pressures larger than ~0.15 Torr. During these micropulses, TDMAZ is reacting with ZrOH* surface species to produce $ZrN(CH_3)^*$ surface species and $HN(CH_3)_2$ as the by-product. Pressures higher than ~0.15 Torr indicate that more $HN(CH_3)_2$ is produced than TDMAZ is lost during the TDMAZ reaction. These higher pressures suggest that many TDMAZ molecules react with two ZrOH* surface groups to release two $HN(CH_3)_2$ products. The saturation behavior for TDMAZ was similar during later ALD cycles.

The pressure then decreases during the repeating TDMAZ micropulses because ZrOH* surface species are progressively consumed by the TDMAZ reaction. The subsequent micropulses labeled "Saturation" in Fig. 6(a) had constant pressures of ~0.15 Torr. These constant pressures indicate that the TDMAZ reaction has reached

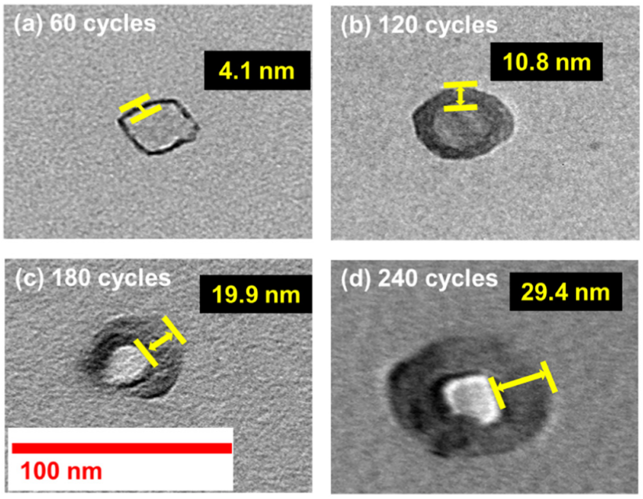

FIG. 7. TEM images of TiO_2/ZrO_2 core/shell nanoparticles after (a) 60, (b) 120, (c) 180, and (d) 240 cycles of ZrO_2 ALD.

saturation. All the $ZrOH^*$ surface species have reacted, and there is no more release of $HN(CH_3)_2$ products.

Micropulses of H_2O were utilized to observe the H_2O reaction with the $ZrN(CH_3)_2{}^*$ surface species that remain after the TDMAZ reaction. Figure 6(b) shows the pressure during these H_2O micropulses. These results were also obtained during the 45th ALD cycle. The first two micropulses are labeled "Reaction." These H_2O micropulses are consistent with H_2O reacting with a $ZrN(CH_3)_2{}^*$ surface species to produce $ZrOH^*$ surface species and $HN(CH_3)_2$ as the product. The pronounced change in the pressure transient between the first and second H_2O micropulses argues that the H_2O reaction almost reaches completion after the second H_2O micropulse.

The nearly identical last two doses with an H_2O pressure of ~0.5 Torr are consistent with the completion of the H_2O reaction on the nanoparticles. These two H_2O micropulses are labeled "Saturation" in Fig. 6(b). The shape of the pressure transient indicates that H_2O is slowly adsorbed by the nanoparticles. However, there is no significant change in the pressure transient between the two H_2O micropulses. This behavior suggests that the H_2O reaction has reached saturation. Similar saturation behavior for H_2O was observed during later ALD cycles.

C. ALD on TiO_2/ZrO_2 core/shell nanoparticles

Figure 7 shows the growth of the ZrO_2 ALD film thickness on the nanoparticles using TDMAZ and H_2O as the reactants at 200 °C. The TDMAZ and H_2O exposures were sufficient for the reactions to reach completion during the TDMAZ and H_2O exposures. ZrO_2 ALD was conducted for up to 240 ALD cycles. Samples were removed from the rotary reactor after every 60 cycles for TEM characterization to monitor the ZrO_2 film thickness.

Figure 7 displays the TEM images of the ZrO_2 ALD film on the TiO_2/ZrO_2 core/shell nanoparticles after 60, 120, 180, and 240 ZrO_2 ALD cycles. The ZrO_2 ALD film grows visibly versus the number of the ZrO_2 ALD cycles. After 60, 120, 180, and 240 ALD cycles, the ZrO_2 shell thickness was 4.1, 10.8, 19.9, and 29.4 nm, respectively, based on the individual TEM measurements shown in

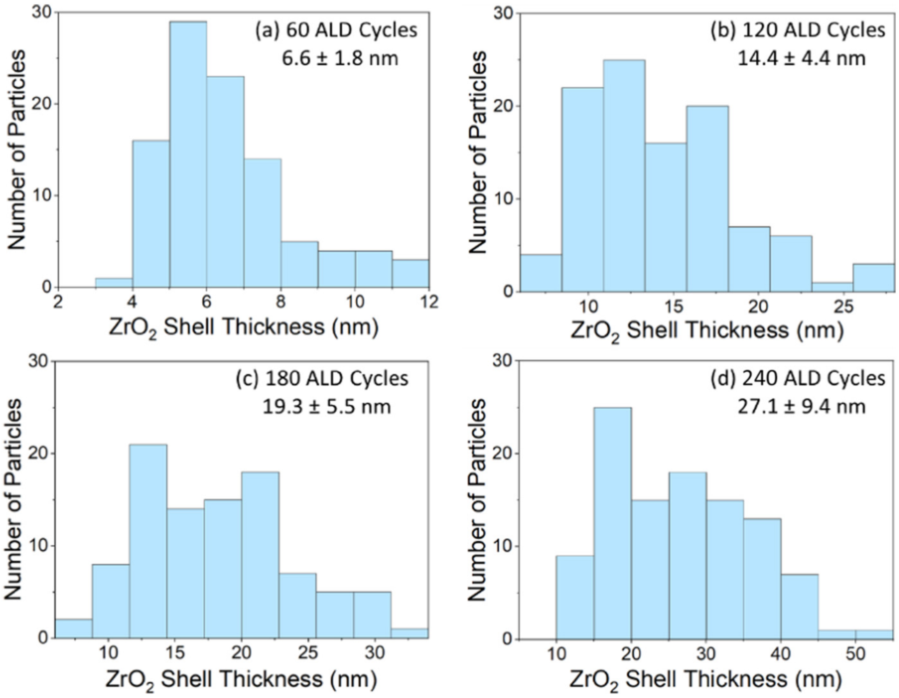

FIG. 8. Histograms for ZrO_2 shell thickness for 100 TiO_2/ZrO_2 core/shell nanoparticles after (a) 60, (b) 120, (c) 180, and (d) 240 ZrO_2 ALD cycles.

Fig. 7. Obtaining growth rates is not possible by comparing individual particles. The growth rates must be determined using the average ZrO_2 shell thicknesses obtained from measurements over many particles.

Histogram distributions of the ZrO_2 shell thickness for 100 nanoparticles are shown in Fig. 8 for (a) 60, (b) 120, (c) 180, and (d) 240 ALD cycles. The ZrO_2 shell thickness increases with ZrO_2 ALD cycles. The ZrO_2 shell thicknesses based on TEM measurements averaged over 100 nanoparticles were 6.6 ± 1.8, 14.4 ± 4.4, 19.3 ± 5.5, and 27.1 ± 9.4 nm, respectively. The ZrO_2 shell thickness distribution also increases with a larger number of ZrO_2 ALD cycles. However, the ratio of the standard deviation of the shell thickness to the average shell thickness after various numbers of ZrO_2 ALD cycles is nearly constant at ∼0.3.

The average ZrO_2 shell thickness versus the number of ZrO_2 ALD cycles is displayed in Fig. 9. There is an initial nucleation delay during the first ∼60 ALD cycles. This nucleation delay may be related to the initial surface composition of the TiO_2/ZrO_2 core/shell nanoparticles prepared by Nanoshel. The TiO_2/ZrO_2 core/shell nanoparticles were used as-received without any further preparation such as high temperature treatment. As mentioned above, XPS analysis revealed adventitious carbon and other surface contaminants such as Na, Fe, and Cl.

A straight line was fit through the average ZrO_2 shell thickness shown in Fig. 9. The linear fit to the ZrO_2 shell thickness versus the number of ZrO_2 ALD cycles yields a ZrO_2 ALD growth rate of 0.9 ± 0.1 Å/cycle. The error bars on the individual points were defined by the standard deviation of the ZrO_2 shell thickness measurements. The growth rate of 0.9 Å/cycle is very similar to the reported growth rate of 0.8 Å/cycle for ZrO_2 ALD on a silicon wafer at 225 °C.[31] A growth rate of 0.9 Å/cycle was also measured for ZrO_2 ALD on graphene nanosheets at 200 °C.[47]

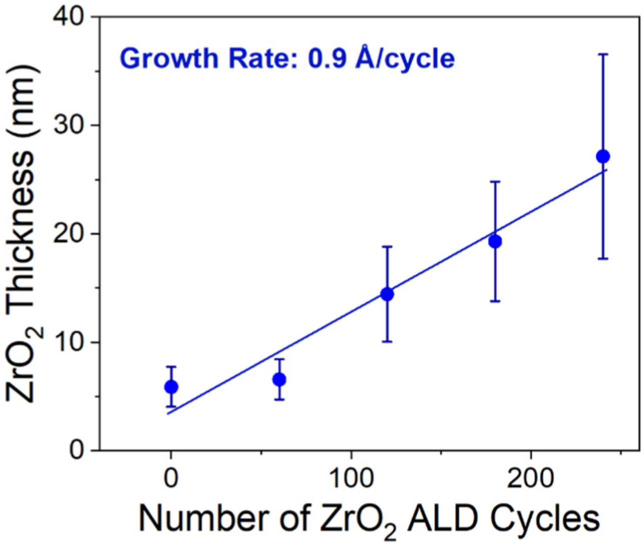

FIG. 9. ZrO_2 thickness vs number of ZrO_2 ALD cycles. ZrO_2 growth rate was 0.9 ± 0.1 Å/cycle.

The growth rate of 0.9 Å/cycle is much less than the thickness of one ZrO_2 monolayer. The density of ZrO_2 is 5.68 g/cm^3, and the molar mass of ZrO_2 is 123.2 g/mol. Consequently, the number density of ZrO_2 is $\rho = 2.78 \times 10^{22}$ ZrO_2 units/cm^3. Assuming a square lattice of ZrO_2 units, the thickness of one ZrO_2 monolayer is $\rho^{-1/3} = 3.3 \times 10^{-8}$ cm = 3.3 Å.

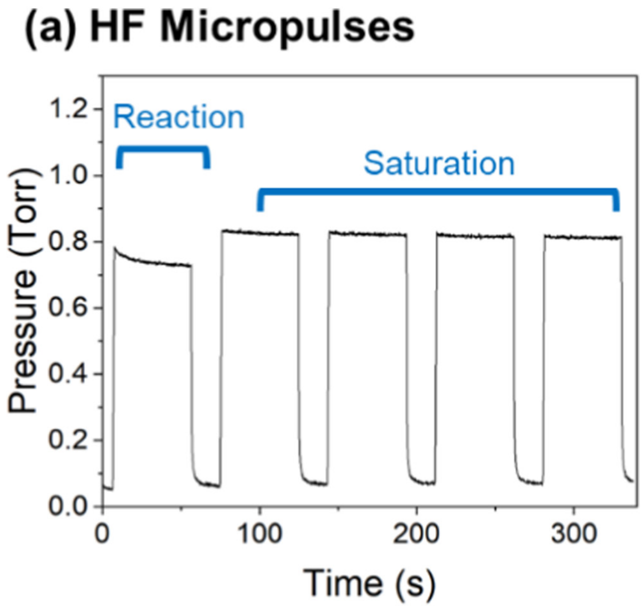

(b) $TiCl_4$ Micropulses

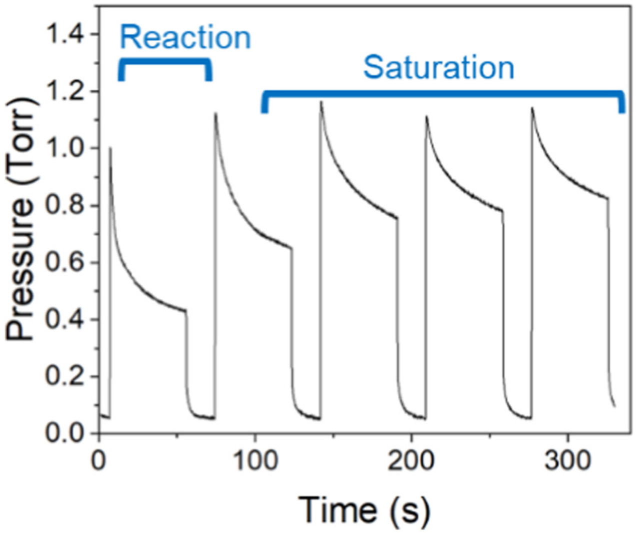

FIG. 10. Transient pressure measurements for multiple micropulses during ZrO_2 ALE at 200 °C during the tenth ALE cycle showing reaction and saturation regimes for (a) HF and (b) $TiCl_4$.

The as-received TiO_2/ZrO_2 core/shell nanoparticles have ZrO_2 shells on crystalline and irregular TiO_2 cores. The TEM images in Fig. 7 visually reveal that ZrO_2 ALD leads to more spherical ZrO_2 shells that envelope the underlying TiO_2 cores. ZrO_2 ALD is smoothing the initial TiO_2/ZrO_2 core/shell nanoparticles and producing more spherical composite nanoparticles. Earlier experiments demonstrated that ALD can smooth initial surface roughness.[48,49] This smoothing by ZrO_2 ALD would also be expected to fill in any gaps in the initial ZrO_2 ALD shell.

The ZrO_2 ALD also does not lead to the TiO_2/ZrO_2 core/shell nanoparticles sticking together to form agglomerates. The TEM images indicate that the nanoparticles remain separate and distinct from one another during ZrO_2 ALD. These observations indicate that the surface chemistry during ZrO_2 ALD does not cause the agglomeration of the TiO_2/ZrO_2 core/shell nanoparticles.

D. Pressure measurements during ZrO_2 ALE

Pressure measurements were also conducted during ZrO_2 ALE. The HF micropulse dosing during HF exposure on the TiO_2/ZrO_2 core/shell particles at 200 °C is shown in Fig. 10(a). These results were obtained during the tenth ALE cycle. Repetitive micropulses of HF at ~0.8 Torr were used for these pressure measurements. The first HF micropulse is reacting with the ZrOH* terminated surface to produce a ZrF_4 surface layer and H_2O as the by-product. The first HF micropulse shows a decrease in the pressure following the initial introduction of HF. Pressures lower than ~0.8 Torr indicate that more HF is adsorbing onto the surface than H_2O is being formed and leaving the surface. The following HF micropulse doses show no change in pressure versus time indicating the saturation of the HF reaction.

Similar $TiCl_4$ micropulse dosing on the TiO_2/ZrO_2 core/shell particles is shown in Fig. 10(b). These results were again obtained during the 10th ALE cycle. Repetitive micropulses of $TiCl_4$ at ~0.7 Torr were used for these pressure measurements. The first micropulse is labeled "Reaction" and is consistent with $TiCl_4$ reacting with the ZrF_4 surface layer to produce $ZrCl_4$ and TiF_4 or TiF_xCl_y as the by-products. The reaction then goes to saturation during the subsequent $TiCl_4$ micropulses labeled "Saturation."

E. ALE on TiO_2/ZrO_2 core/shell nanoparticles

The ZrO_2 films on the TiO_2/ZrO_2 core/shell nanoparticles were etched in the rotary reactor using ZrO_2 ALE at 200 °C. The ZrO_2 ALE was performed using sequential exposures of HF and $TiCl_4$. The reaction sequence was four HF micropulses at ~0.8 Torr for 0.3 s, N_2 purge for 230 s, four $TiCl_4$ micropulses at ~1 Torr for 0.3 s, and N_2 purge for 230 s. Samples were removed from the rotary reactor after every 10 cycles for TEM characterization to monitor the ZrO_2 film thickness. The ZrO_2 film thickness was determined by TEM measurements of the ZrO_2 shell thickness of 100 particles from each sample aliquot.

TEM images of the TiO_2/ZrO_2 core/shell nanoparticles after 10, 20, and 30 ZrO_2 ALE cycles are shown in Fig. 11. The ZrO_2 shell thickness decreases progressively versus number of ZrO_2 ALE cycles. The initial TiO_2/ZrO_2 core/shell nanoparticles had an average ZrO_2 shell thickness of 27.1 nm. After 10, 20, and 30 ALE cycles, the ZrO_2 shell thickness was 24.7, 14.3, and 7.7 nm, respectively, based on the individual TEM measurements shown in Fig. 11. Determining the etch rates is not possible by comparing individual particles. The etch rates must be obtained using the average ZrO_2 shell thicknesses derived from measurements over many particles.

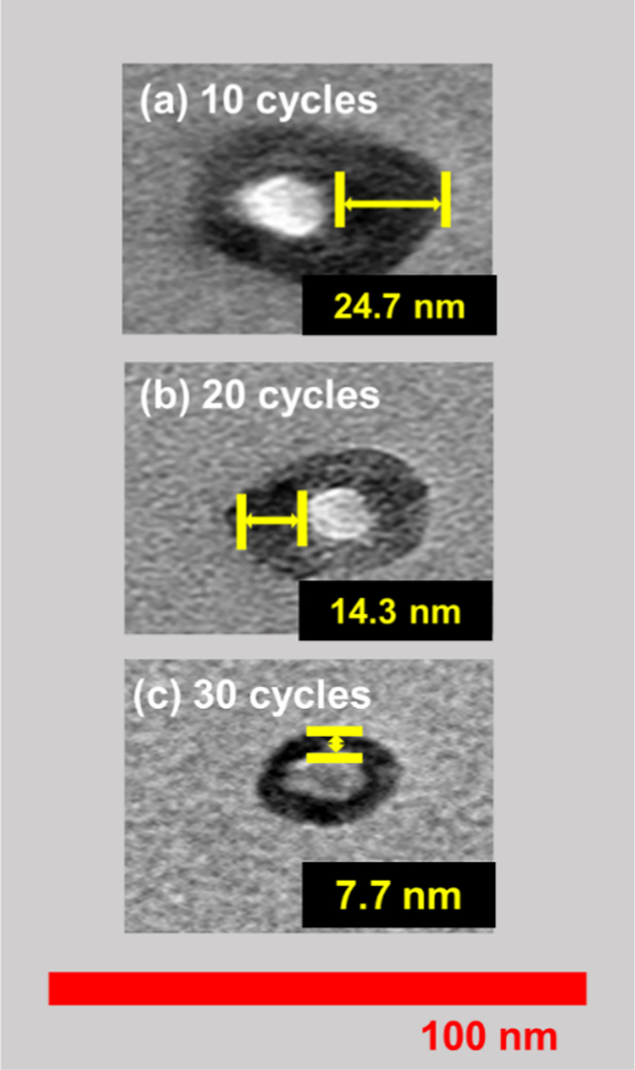

FIG. 11. TEM images of TiO_2/ZrO_2 core/shell nanoparticles after (a) 10, (b) 20, and (c) 30 cycles of ZrO_2 ALE.

Histogram distributions of the ZrO_2 shell thickness for 100 nanoparticles after (a) 10, (b) 20, (c) 30 ALE cycles are shown in Fig. 12. The ZrO_2 shell thickness decreases progressively with ZrO_2 ALE cycles. The ZrO_2 shell thickness based on TEM measurements averaged over 100 nanoparticles was 20.6 ± 7.6, 13.4 ± 3.2, and 7.6 ± 2.4 nm, respectively. The ZrO_2 shell thickness distribution also decreases with ZrO_2 ALE cycles. In similarity with the results for ZrO_2 ALD in Fig. 8, the ratio of the standard deviation of

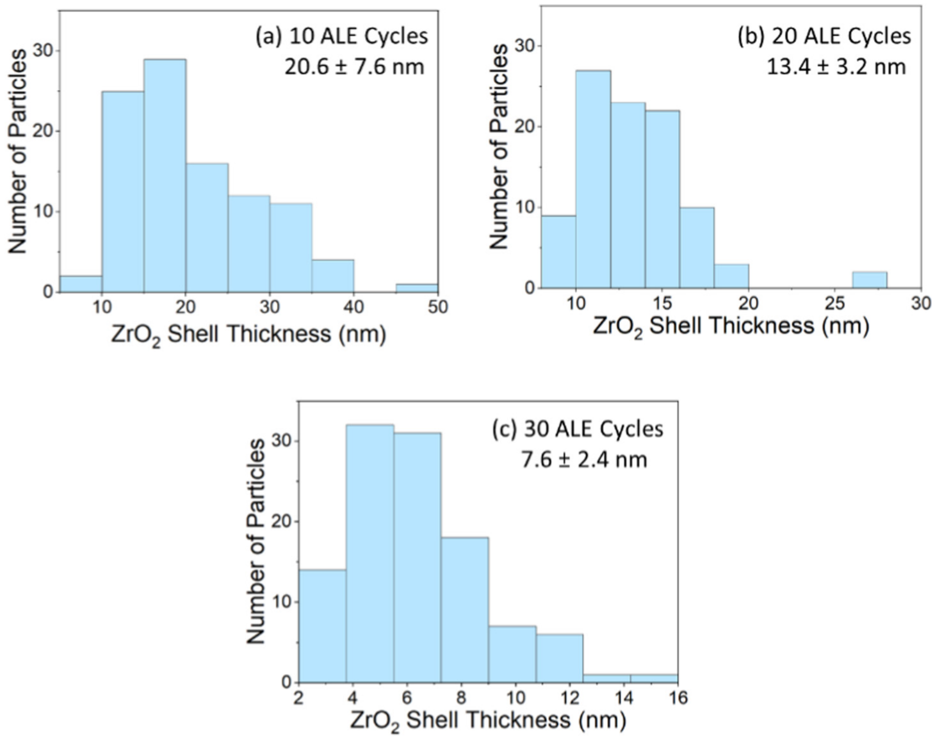

FIG. 12. Histograms for the ZrO_2 shell thickness for 100 TiO_2/ZrO_2 core/shell nanoparticles after (a) 10, (b) 20, and (c) 30 ZrO_2 ALE cycles.

the shell thickness and the average shell thickness after the various number of ZrO_2 ALE cycles remains nearly constant at ~0.3.

Figure 13 shows the TEM measurements for the ZrO_2 film thickness on the TiO_2/ZrO_2 core/shell nanoparticles versus number of ZrO_2 ALE cycles. A straight line was fit through the average ZrO_2 shell thicknesses displayed in Fig. 13. The linear fit to the ZrO_2 shell thickness versus number of ZrO_2 ALE cycles yields a ZrO_2 ALE etch rate of 6.5 ± 0.2 Å/cycle. The error bars on the individual points were defined by the standard deviation of the ZrO_2 shell thickness measurements.

The etch rate of 6.5 ± 0.2 Å/cycle is significantly larger than earlier reported etch rates. A previous study explored ZrO_2 ALE at 250 °C using HF and $TiCl_4$ as the precursors for flat amorphous and crystalline ZrO_2 films.[37] The amorphous ZrO_2 had an etch rate of 0.61 Å/cycle, and the crystalline ZrO_2 had an etch rate of 0.26 Å/cycle.[37] The differences between the particle etching and the flat film etching could be attributed to the reactant exposure conditions. The current study on nanoparticles used static reactant exposures with pressures of 0.3–1.0 Torr. The previous study on flat films used viscous flow exposures with much lower pressures of 80–120 mTorr. Higher HF pressures and exposures could lead to a thicker ZrF_4 surface layer and larger ZrO_2 etch rates as observed earlier for Al_2O_3 ALE.[50]

Another factor that could increase the etch rate of the ZrO_2 shell on the TiO_2/ZrO_2 core/shell nanoparticles is the particle curvature. Atomic layer etching is known to smooth amorphous metal oxide surfaces.[48,51–53] One possible mechanism for surface smoothing is the preferential fluorination of lower radius of curvature surface areas.[37,48] The fluorination of crystalline ZrO_2 to crystalline ZrF_4 involves a volume expansion of 1.74.[37] The lower radius of curvature surface areas may be able to expand more easily to accommodate the volume expansion upon fluorination. The thicker fluoride layers for the lower radius of curvature surfaces may then yield larger etch rates.

The TEM measurements in Fig. 7 show that the ZrO_2 shell is smooth and spherical on the starting TiO_2/ZrO_2 core/shell nanoparticles after ZrO_2 ALD. Figure 11 reveals that the ZrO_2 shell that surrounds the underlying TiO_2 core remains smooth and spherical after the various number of ZrO_2 ALE cycles. This behavior is expected because earlier studies have shown that ALE can smooth the surface roughness of amorphous ALD films as mentioned above.[48,51–53] Consequently, after the ZrO_2 ALD fills any gaps in the initial ZrO_2 shell and smooths the surface roughness of the initial TiO_2 core nanoparticle, the ZrO_2 ALE retains the spherical ZrO_2 shell on the TiO_2 core nanoparticle.

The ZrO_2 ALE also does not cause the TiO_2/ZrO_2 core/shell nanoparticles to stick together to form agglomerates. The TEM images show that the nanoparticles remain separate and distinct from one another during ZrO_2 ALE. These observations indicate that the surface reactions during ZrO_2 ALE do not lead to the agglomeration of the TiO_2/ZrO_2 core/shell nanoparticles.

F. Mass spectrometry studies

QMS was used to identify the volatile etch products during the etching of ZrO_2 by sequential HF and $TiCl_4$ exposures. For these QMS studies, the reactants were exposed to ZrO_2

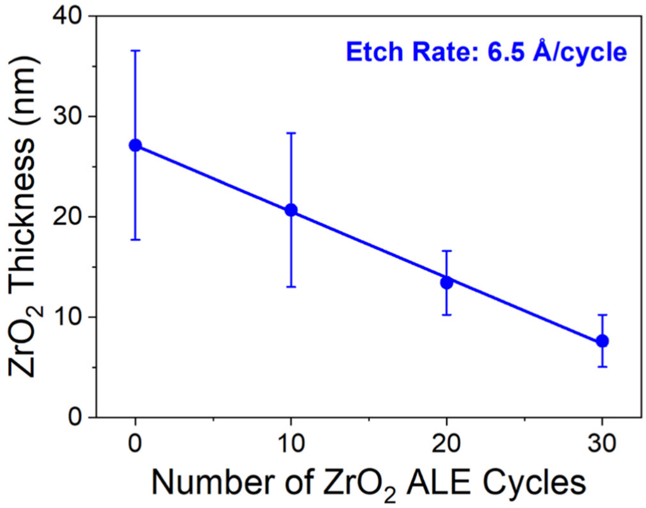

FIG. 13. ZrO_2 thickness vs number of ZrO_2 ALE cycles. ZrO_2 etch rate was 6.5 ± 0.2 Å/cycle.

powder in the QMS reactor at 200, 250, and 300 °C. Figure 14 displays the time-resolved QMS signals during a $TiCl_4$/HF/$TiCl_4$/HF/$TiCl_4$ exposure sequence at the three temperatures. The reaction sequence was 120 s for each reactant exposure followed by a 300 s N_2 purge. Etch products were observed at all three temperatures with the signal intensity increasing at higher temperatures.

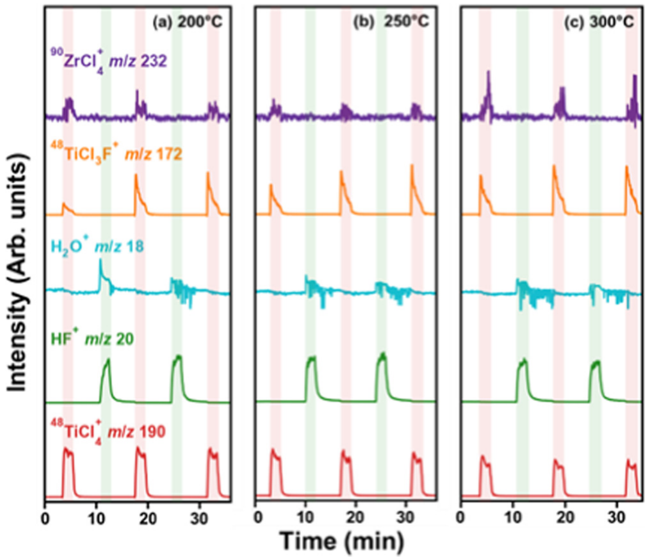

FIG. 14. Time-dependent QMS results during sequential HF and $TiCl_4$ exposures on ZrO_2 powder showing ion signal intensities for $ZrCl_4^+$ at *m/z* 232, $TiClF_3^+$ at *m/z* 172, H_2O^+ at *m/z* 18, HF^+ at *m/z* 20, and $TiCl_4^+$ at *m/z* 190. Temperatures were (a) 200, (b) 250, and (c) 300 °C.

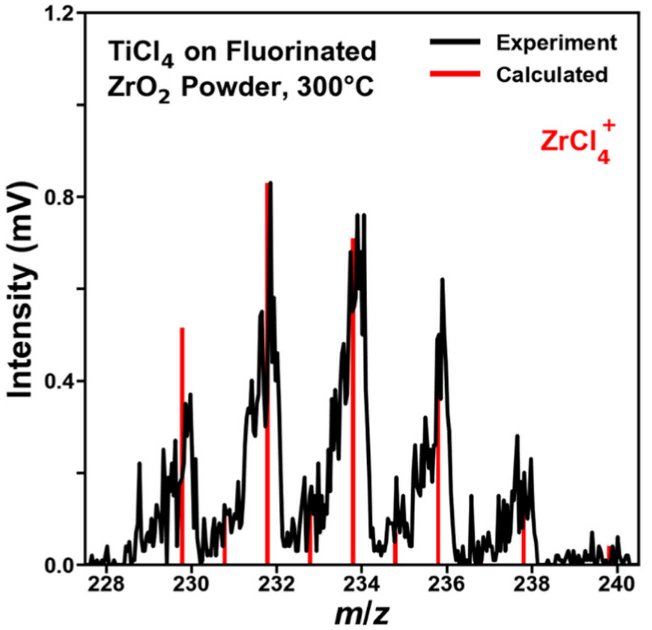

FIG. 15. Mass spectrum of the $ZrCl_4^+$ ion signal during $TiCl_4$ exposure on fluorinated ZrO_2 powder. Experimental spectrum agrees with calculated spectrum based on natural isotopic abundance of elements.

The H_2O^+ ion intensity at *m/z* 18 is observed in Fig. 14 when HF is exposed to the ZrO_2 powder. An H_2O^+ ion signal at *m/z* 18 is expected when HF fluorinates ZrO_2 to produce a ZrF_4 surface layer and H_2O. The fluorination reaction is

$$ZrO_2 + 4HF(g) \rightarrow ZrF_4 + 2H_2O(g).$$

Figure 14 also shows that a $ZrCl_4^+$ ion signal at *m/z* 232 from the $ZrCl_4$ etch product is observed when $TiCl_4$ is exposed to the fluorinated ZrO_2 powder. The $ZrCl_4$ etch product is anticipated based on the ligand-exchange reaction of $TiCl_4$ with the ZrF_4 surface layer. The reaction product after four ligand-exchange events between the same Zr and Ti metal centers is

$$ZrF_4 + TiCl_4(g) \rightarrow ZrCl_4(g) + TiF_4(g).$$

The reaction of $TiCl_4$ with the fluorinated ZrO_2 powder could also lead to other various $TiCl_xF_y$ reaction products. One possibility is ligand-exchange between the Zr metal center and four different $TiCl_4$ reactants. The ligand-exchange reaction for four different $TiCl_4$ reactants with the same Zr metal center is

$$ZrF_4 + 4TiCl_4(g) \rightarrow ZrCl_4(g) + 4TiFCl_3(g).$$

Figure 14 reveals that the QMS results observe a $TiFCl_3^+$ ion signal at *m/z* 172 during the $TiCl_4$ reactant exposures. This $TiFCl_3^+$ ion signal is derived from one ligand-exchange reaction between $TiCl_4$ and the fluorinated ZrO_2 surface. Additional QMS measurements revealed that the $TiFCl_3^+$ ion signal increased quickly at the beginning of the $TiCl_4$ exposure. The decrease in the $TiFCl_3^+$ ion signals also occurred, while the $TiCl_4^+$ ion signal remained constant. This behavior indicates a self-limiting ALE reaction.

The identity of the $ZrCl_4^+$ ion signal can be confirmed based on the agreement between the experimental mass spectrum and the mass spectrum predicted from the natural abundances of the isotopes of the elements in $ZrCl_4$. Chlorine has two main isotopes (^{35}Cl and ^{37}Cl). Zirconium has four main isotopes (^{90}Zr, ^{91}Zr, ^{92}Zr, and ^{94}Zr). Figure 15 shows the mass spectrum from *m/z* 228 to *m/z* 240 during $TiCl_4$ exposure on fluorinated ZrO_2 powder at 300 °C. There is an excellent agreement between the ion signals at the different masses and the calculated spectrum for $ZrCl_4^+$ based on the isotopic natural abundances for Zr and Cl.

IV. CONCLUSIONS

This study provided a demonstration that ZrO_2 ALD and ZrO_2 ALE can tune the thickness of ZrO_2 shells on TiO_2/ZrO_2 core/shell nanoparticles. To increase the shell thickness, ZrO_2 ALD was performed using TDMAZ and H_2O as the reactants in a rotary reactor. Starting with TiO_2/ZrO_2 core/shell nanoparticles, ZrO_2 ALD added ZrO_2 thickness at 0.9 ± 0.1 Å per ALD cycle. Pressure measurements during multiple micropulses were employed to determine the conditions for self-limiting TDMAZ and H_2O reactions during ALD. The ZrO_2 ALD produced more spherical ZrO_2 shells on the crystalline TiO_2 core of the nanoparticles. The ZrO_2 ALD occurred without causing agglomeration of the TiO_2/ZrO_2 core/shell nanoparticles.

To decrease the shell thickness, ZrO_2 ALE was conducted using HF and $TiCl_4$ as the reactants in the rotary reactor. ZrO_2 ALE removed ZrO_2 with an etch rate of 6.5 ± 0.2 Å per ALE cycle. The conditions for self-limiting HF and $TiCl_4$ ALE reactions were determined using pressure measurements during multiple micropulses. The spherical ZrO_2 shells were maintained during ZrO_2 ALE. In addition, the ZrO_2 ALE occurred without causing agglomeration of the TiO_2/ZrO_2 core/shell nanoparticles. QMS experiments also identified the main products during ZrO_2 ALE. H_2O was observed during HF exposures. $ZrCl_4$ and $TiFCl_3$ were monitored during $TiCl_4$ exposures.

This combined ALD and ALE method provides the Ångstrom–level control of the ZrO_2 shell thickness on TiO_2/ZrO_2 core/shell nanoparticles. In addition, more continuous ZrO_2 shells are possible because ZrO_2 ALD smooths the surface and leads to spherical shells. ZrO_2 ALE then reduces the film thickness and maintains the smooth spherical shell. Because the ZrO_2 ALD and ZrO_2 ALE can occur without particle agglomeration, this method should be useful to prepare TiO_2/ZrO_2 core/shell nanoparticles for many applications including TiO_2/polymer composites.

ACKNOWLEDGMENTS

This research was funded by Meta Reality Labs in Redmond, Washington. Funding for the QMS reactor and the QMS investigations was provided by Lam Research. The authors thank Garry Morgan from the Boulder Electron Microscopy Services for TEM training and support. The authors also thank Andrew S. Cavanagh for performing the XPS analysis.

AUTHOR DECLARATIONS

Conflict of Interest

The authors have no conflicts to disclose.

Author Contributions

Janine D. Sempel: Data curation (equal); Formal analysis (lead); Investigation (equal); Writing – original draft (lead); Writing – review & editing (supporting). **Marja-Leena Kaariainen:** Data curation (equal); Formal analysis (supporting); Investigation (equal); Writing – original draft (supporting); Writing – review & editing (supporting). **Troy A. Colleran:** Data curation (supporting); Investigation (supporting); Writing – original draft (supporting); Writing – review & editing (supporting). **Alejo M. Lifschitz:** Conceptualization (supporting); Funding acquisition (equal); Project administration (supporting); Supervision (supporting); Writing – review & editing (supporting). **Steven M. George:** Conceptualization (lead); Funding acquisition (equal); Methodology (lead); Project administration (lead); Supervision (lead); Writing – review & editing (lead).

DATA AVAILABILITY

The data that support the findings of this study are available within the article.

REFERENCES

[1] R. G. Chaudhuri and S. Paria, Chem. Rev. **112**, 2373 (2012).
[2] F. Caruso, Adv. Mater. **13**, 11 (2001).
[3] K. Chatterjee, S. Sarkar, K. J. Rao, and S. Paria, Adv. Colloid Interface Sci. **209**, 8 (2014).
[4] M. B. Gawande, A. Goswami, T. Asefa, H. Z. Guo, A. V. Biradar, D. L. Peng, R. Zboril, and R. S. Varma, Chem. Soc. Rev. **44**, 7540 (2015).
[5] S. J. Oldenburg, R. D. Averitt, S. L. Westcott, and N. J. Halas, Chem. Phys. Lett. **288**, 243 (1998).
[6] P. Reiss, M. Protiere, and L. Li, Small **5**, 154 (2009).
[7] G. Nichols, S. Byard, M. J. Bloxham, J. Botterill, N. J. Dawson, A. Dennis, V. Diart, N. C. North, and J. D. Sherwood, J. Pharm. Sci. **91**, 2103 (2002).
[8] S. M. George, Chem. Rev. **110**, 111 (2010).
[9] A. W. Weimer, J. Nanopart. Res. **21**, 9 (2019).
[10] J. D. Ferguson, A. W. Weimer, and S. M. George, Thin Solid Films **371**, 95 (2000).
[11] J. D. Ferguson, A. W. Weimer, and S. M. George, Chem. Mater. **12**, 3472 (2000).
[12] J. D. Ferguson, A. W. Weimer, and S. M. George, Chem. Mater. **16**, 5602 (2004).
[13] J. D. Ferguson, A. R. Yoder, A. W. Weimer, and S. M. George, Appl. Surf. Sci. **226**, 393 (2004).
[14] J. R. Wank, S. M. George, and A. W. Weimer, J. Am. Ceram. Soc. **87**, 762 (2004).
[15] J. D. Ferguson, A. W. Weimer, and S. M. George, Thin Solid Films **413**, 16 (2002).
[16] J. C. Gertsch, E. Sortino, V. M. Bright, and S. M. George, J. Vac. Sci. Technol. A **39**, 062602 (2021).
[17] S. M. George, Acc. Chem. Res. **53**, 1151 (2020).
[18] T. Faraz, F. Roozeboom, H. C. M. Knoops, and W. M. M. Kessels, ECS J. Solid State Sci. Technol. **4**, N5023 (2015).
[19] A. Fischer, A. Routzahn, S. M. George, and T. Lill, J. Vac. Sci. Technol. A **39**, 030801 (2021).
[20] O. Carp, C. L. Huisman, and A. Reller, Prog. Solid State Chem. **32**, 33 (2004).
[21] X. Chen and S. S. Mao, Chem. Rev. **107**, 2891 (2007).
[22] U. Diebold, Surf. Sci. Rep. **48**, 53 (2003).

[23] Y. Wang, J. Zhang, X. Y. Shen, C. N. Shi, J. J. Wu, and L. Sun, Mater. Chem. Phys. **98**, 217 (2006).
[24] N. Nakayama and T. Hayashi, J. Appl. Polym. Sci. **105**, 3662 (2007).
[25] M. Takafuji, M. Kajiwara, N. Hano, Y. Kuwahara, and H. Ihara, Nanomaterials **9**, 514 (2019).
[26] P. Tao, Y. Li, A. Rungta, A. Viswanath, J. N. Gao, B. C. Benicewicz, R. W. Siegel, and L. S. Schadler, J. Mater. Chem. **21**, 18623 (2011).
[27] S. M. Cho and W. Y. Choi, J. Photochem. Photobiol., A **143**, 221 (2001).
[28] R. E. Day, Polym. Degrad. Stab. **29**, 73 (1990).
[29] T. J. Kemp and R. A. McIntyre, Prog. React. Kinet. Mech. **26**, 337 (2002).
[30] D. M. Hausmann, E. Kim, J. Becker, and R. G. Gordon, Chem. Mater. **14**, 4350 (2002).
[31] X. Wang, S. Ghosh, M. Afshar-Mohajer, H. Zhou, Y. Q. Liu, X. X. Han, J. Y. Cai, M. Zou, and X. B. Meng, J. Mater. Res. **35**, 804 (2020).
[32] S. E. Jo, S. Jeon, H. J. Kim, B. C. Yang, K. Ju, T. M. Gür, W. Jung, and J. An, Small Methods **8**, 2300790 (2024).
[33] W. Y. Lin *et al.*, Appl. Surf. Sci. **615**, 156278 (2023).
[34] T. M. Onn, S. Y. Zhang, L. Arroyo-Ramirez, Y. C. Chung, G. W. Graham, X. Q. Pan, and R. J. Gorte, ACS Catal. **5**, 5696 (2015).
[35] L. F. Rasteiro, A. Motin, L. H. Vieira, E. M. Assaf, and F. Zaera, Thin Solid Films **768**, 139716 (2023).
[36] Y. Lee and S. M. George, J. Vac. Sci. Technol. A **36**, 061504 (2018).
[37] J. A. Murdzek and S. M. George, J. Vac. Sci. Technol. A **38**, 022608 (2020).
[38] J. A. McCormick, B. L. Cloutier, A. W. Weimer, and S. M. George, J. Vac. Sci. Technol. A **25**, 67 (2007).
[39] J. A. McCormick, K. P. Rice, D. F. Paul, A. W. Weimer, and S. M. George, Chem. Vap. Deposition **13**, 491 (2007).
[40] J. W. Clancey, A. S. Cavanagh, R. S. Kukreja, A. Kongkanand, and S. M. George, J. Vac. Sci. Technol. A **33**, 01a130 (2015).
[41] A. Lii-Rosales, A. S. Cavanagh, A. Fischer, T. Lill, and S. M. George, Chem. Mater. **33**, 7719 (2021).
[42] J. L. Partridge, J. A. Murdzek, V. L. Johnson, A. S. Cavanagh, A. Fischer, T. Lill, S. Sharma, and S. M. George, Chem. Mater. **35**, 2058 (2023).
[43] T. A. Egerton and I. R. Tooley, Int. J. Cosmet. Sci. **36**, 195 (2014).
[44] D. X. Zhou, Z. X. Ji, X. M. Jiang, D. R. Dunphy, J. Brinker, and A. A. Keller, PLoS One **8**, e81239 (2013).
[45] G. Li, L. Lv, H. T. Fan, J. Y. Ma, Y. Q. Li, Y. Wan, and X. S. Zhao, J. Colloid Interface Sci. **348**, 342 (2010).
[46] S. Murugadoss *et al.*, Part. Fibre Toxicol. **17**, 10 (2020).
[47] J. Liu, X. B. Meng, Y. H. Hu, D. S. Geng, M. N. Banis, M. Cai, R. Y. Li, and X. L. Sun, Carbon **52**, 74 (2013).
[48] S. H. Gerritsen, N. J. Chittock, V. Vandalon, M. A. Verheijen, H. C. M. Knoops, W. M. M. Kessels, and A. J. M. Mackus, ACS Appl. Nano Mater. **5**, 18116 (2022).
[49] T. J. Myers, J. A. Throckmorton, R. A. Borrelli, M. O'Sullivan, T. Hatwar, and S. M. George, Appl. Surf. Sci. **569**, 150878 (2021).
[50] A. M. Cano, A. E. Marquardt, J. W. DuMont, and S. M. George, J. Phys. Chem. C **123**, 10346 (2019).
[51] A. I. Abdulagatov and S. M. George, J. Vac. Sci. Technol. A **38**, 022607 (2020).
[52] Y. Lee, J. W. DuMont, and S. M. George, ECS J. Solid State Sci. Technol. **4**, N5013 (2015).
[53] D. R. Zywotko, J. Faguet, and S. M. George, J. Vac. Sci. Technol. A **36**, 061508 (2018).